Molecular dynamics simulation of electro-osmotic flows in rough wall nanochannels

Daejoong Kim* and Eric Darve
Department of Mechanical Engineering, Stanford University, Stanford, California 94305, USA
(Received 7 June 2005; revised manuscript received 6 January 2006; published 9 May 2006)

We performed equilibrium and nonequilibrium molecular dynamics simulation to study electro-osmotic flows inside charged nanochannels with different types of surface roughness. We modeled surface roughness as a sequence of two-dimensional subnanoscale grooves and ridges (step function-type roughness) along the flow direction. The amplitude, spatial period, and symmetry of surface roughness were varied. The amplitude of surface roughness was on the order of the Debye length. The walls have uniform negative charges at the interface with fluids. We included only positive ions (counterions) for simplicity of computation. For the smooth wall, we compared our molecular dynamics simulation results to the well-known Poisson-Boltzmann theory. The density profiles of water molecules showed "layering" near the wall. For the rough walls, the density profiles measured from the wall are similar to those for the smooth wall except near where the steps are located. Because of the layering of water molecules and the finite size effect of ions and the walls, the ionic distribution departs from the Boltzmann distribution. To further understand the structure of water molecules and ions, we computed the polarization density. Near the wall, its z component dominates the other components, indicating the preferred orientation ("ordering") of water molecules. Especially, inside the groove for the rough walls, its maximum is 10% higher (stronger ordering) than for the smooth wall. The dielectric constant, computed with a Clausius-Mosotti-type equation, confirmed the ordering near the wall and the enhanced ordering inside the groove. The residence time and the diffusion coefficient, computed using the velocity autocorrelation function, showed that the diffusion of water and ions along the direction normal to the wall is significantly reduced near the wall and further decreases inside the groove. Along the flow direction, the diffusion of water and ions inside the groove is significantly lowered while it is similar to the bulk value elsewhere. We performed nonequilibrium molecular dynamics simulation to compute electro-osmotic velocities and flow rates. The velocity profiles correspond to those for overlapped electric double layers. For the rough walls, velocity inside the groove is close to zero, meaning that the channel height is effectively reduced. The flow rate was found to decrease as the period of surface roughness decreases or the amplitude of surface roughness increases. We defined the ζ potential as the electrostatic potential at the location of a slip plane. We computed the electrostatic potential with the ionic distribution and the dielectric constant both from our molecular dynamics simulation. We estimated the slip plane from the velocity profile. The ζ potential showed the same trend as the flow rate: it decreases with an increasing amplitude and a decreasing period of surface roughness.

DOI: 10.1103/PhysRevE.73.051203 PACS number(s): 66.10.Ed, 68.08.De

I. INTRODUCTION

Flow physics at nanoscale has gained increasing attention in recent years. This nanofluidics is of fundamental scientific interest as well as of engineering interest due to the possibility of practical applications in many fields, for example, separation and identification of biological and chemical species. To understand nanoscale fluid phenomena, many experimental and computational research efforts have been taken. Experimentally, nanochannels of various sizes with different materials have been fabricated and studied [1–7]. Various types of simulation techniques have been used, ranging from continuum models to atomistic simulation [8–13].

One prominent difference between the fluid motions in nanochannels and those in macroscale channels is the strong fluid-wall interactions observed in nanochannels. As the channel size decreases, the surface-to-volume ratio increases. Therefore, various properties of the walls, such as surface roughness, greatly affect the fluid motions in nanochannels. Although laminar flows have been known to be only slightly influenced by surface roughness in macroscale channels [14], the effect of surface roughness is expected to be significant in nanochannels. Indeed, the amplitude of surface roughness is only one or two orders of magnitude lower than the channel height for many nanochannels. Many studies considered the effect of surface roughness on nanoscale flows. Specifically, its effect on slip phenomena has been experimentally and computationally reported in many papers. Lauga *et al.* did a recent and complete review on this topic [15]. Karniadakis and Beskok also did an excellent review [16]. We will summarize these papers briefly in Sec. II.

One of the driving forces in nanochannels is electro-osmotic drag [1,2]. Electro-osmotic flows have been studied in many different contexts, including atomistic simulation to study fluid-wall interactions at molecular scale [17–19]. Near a charged wall, an electric double layer, consisting of a Stern layer and a diffuse layer, is formed. When an electric field is applied, electric body forces are exerted on ions accumulated in the electric double layer. By viscous drag due to the moving ions, water molecules are then put into motion. Depending on the ionic strength of the liquids, the electric double layers may extend to the whole channel volume and overlap

*Electronic address: daejoongkim@stanford.edu

[20,21]. While overlapped electric double layers are typically rare in macroscale and microscale channels, it can often be found in nanochannels [1,2].

In recent years, there have been papers on electro-osmotic flows in nanochannels using atomistic simulation. Freund has examined the validity of the continuum-based Poisson-Boltzmann theory by comparing it to his atomistic simulation results [11]. He reported different profiles of the ion density and the water velocity near the walls using the two methods. He also found the preferred orientations of water molecules and their decreased diffusion near the walls. To solve the discrepancy between the continuum and atomistic models, Qiao and Aluru proposed a modified Poisson-Boltzmann (PB) equation supplemented by molecular dynamics simulation [13]. In particular, their modification includes finite size effects of water molecules and ions. In a subsequent paper [22], they simulated more realistic model systems by including coions (ions with charges of the same polarity as in the walls) in their molecular dynamics (MD) simulation. They found "charge inversion," meaning that the direction of electro-osmotic flows is opposite to that predicted by the continuum theory. In their most recent paper [23], they reported different ionic distributions in positively and negatively charged channel walls due to different hydrogen bond patterns, which cannot be observed with the continuum theory. Zhou *et al.* studied electro-osmotic flows in model silica nanopores [12]. They reported that the wall has little effect on the axial movement of water molecules and ions along the nanopore. Joly *et al.* studied the effect of hydrophobicity on electric double layers [24] and found that the ζ potential, a measure of the electro-osmotic velocity at a given applied electric field, is considerably amplified by the existence of slip near hydrophobic walls.

As summarized above, atomistic simulation of electro-osmotic flows in smooth nanochannels (only with atomic roughness) and pressure-driven flows in rough nanochannels has been reported in several reviews and papers. However, we have not found atomistic simulation of electro-osmotic flows in rough nanochannels reported in the literature. In fact, the effects of surface roughness on an electric double layer even in light of continuum models have yet to be studied [25]. Recent related works include continuum simulation of electro-osmotic flows in rough microchannels and in grooved microchannels [26–28]. Although they reported exciting results, their approaches are limited to continuum regime and may fail at nanoscale.

In this paper, we used molecular dynamics (MD) simulation to study electro-osmotic flows in rough nanochannels. We are particularly interested in the interactions between rough walls and fluids at molecular scale; thus, we explicitly accounted for the molecular nature of the walls and the water molecules.

II. THEORY OF AN ELECTRIC DOUBLE LAYER ON SMOOTH AND ROUGH WALLS

In a continuum limit, the structure of an electric double layer on a smooth charged wall can be obtained typically by solving the well-known Poisson-Boltzmann (PB) equation [29]. The PB equation is the Poisson equation [Eq. (1)] for the electrostatic potential, combined with a Boltzmann distribution [Eq. (2)] for the ion density

$$\epsilon \nabla^2 \psi = -\rho_E, \tag{1}$$

$$n_i = n_{\infty,i} \exp\left(-\frac{z_i e \psi}{k_B T}\right), \tag{2}$$

$$\rho_E = \sum_{i=1}^{N} z_i e n_i. \tag{3}$$

The one-dimensional PB equation is

$$\frac{d^2\psi}{dz^2} = -\frac{e}{\epsilon} \sum_{i=1}^{N} z_i n_{\infty,i} \exp\left(-\frac{z_i e \psi(z)}{k_B T}\right). \tag{4}$$

Here ψ is the local electrostatic potential, ρ_E is the charge density measured in coulombs per cubic meter, e is the elementary charge (1.602×10^{-19} C), k_B is the Boltzmann constant (1.381×10^{-23} JK^{-1}), ϵ is the permittivity of medium ($\epsilon = \epsilon_0 \epsilon_r$ where ϵ_0 is the vacuum permittivity, 8.854×10^{-12} J^{-1} C^2 m^{-1}, and ϵ_r is the dielectric constant of medium, 77.8 for water at 300 K and 0.1 MPa [30]), and T is the temperature of medium. The summation should be done for N different species of present ions. $n_{\infty,i}$ is the number density of each ion species in bulk, and z_i is its valence.

For the simplicity of computation, we assumed only one monovalent ion species, which have charges opposite to the wall charge (counterions) to maintain global electroneutrality. In this case, we can reduce Eq. (4) to

$$\frac{d^2\psi}{dz^2} = -\frac{e}{\epsilon} n_\infty \exp\left(-\frac{e\psi(z)}{k_B T}\right). \tag{5}$$

Its analytical solution is

$$\psi(z) = \frac{k_B T}{e} \ln\left[\cos^2 \sqrt{\frac{e^2 n_\infty (z - z_m)^2}{2\epsilon k_B T}}\right], \tag{6}$$

with the convention that $\psi = 0$ at the channel center [31]. Here z_m is the z coordinate of the channel center. In this equation the only unknown is n_∞, and we can find it using appropriate boundary conditions. The boundary condition for the PB equation can be either a Dirichlet condition if the electrostatic potential is known (the ζ potential in this case) or a Neumann condition if the surface charge density is given. In the present context, the appropriate condition is the one with a fixed surface charge density σ. The boundary condition can be formulated as

$$\sigma = \epsilon \frac{d\psi}{dz}(z = z_{\text{wall}}), \tag{7}$$

where σ is the surface charge density measured in coulombs per square meter. Note that σ and ρ_E have different units. A similar type of condition was used in several previous works [1,11,13].

In order to compute electro-osmotic flows, we solved the Stokes equation [Eq. (8)] with an electric body force term obtained from the PB solution

$$\mu \frac{d^2u}{dz^2} = -en_\infty E. \tag{8}$$

Here μ is the viscosity of medium (0.89 mPa for water at 25 °C [30]). The boundary conditions are

$$\frac{du}{dz}(z = z_m) = 0 \tag{9}$$

and

$$u(z = z_{\text{wall}}) = 0. \tag{10}$$

One important notion in this PB approach is the distinction between the surface potential and the ζ potential. The ζ potential can be defined as the electrostatic potential at a slip plane. This distinction is especially important since surface roughness is known to decrease slip [15] and possibly change the location of a slip plane, letting the ζ potential deviate much from the surface potential. The continuum-based PB approach has some imperfections, several of which are listed in Lyklema [29]. One of our purposes in the present study is to examine some of these.

The effects of surface roughness on slip phenomena near uncharged solid walls have been previously studied. In gas flows, the amplitude of surface roughness relative to the channel height and the mean free path is very important for the slip and no-slip conditions [16]. Lauga *et al.* [15] summarized the effects of surface roughness on liquid flows: (i) in some cases it increases fluid friction but in other cases it decreases fluid friction; (ii) it decreases slip; and (iii) it can induce dewetting of solid surfaces.

The structure of electric double layers on charged rough walls has been addressed in several books [29,32,33]. A recent review can be found in Zembala [25]. Bikerman explained both the possibility of increase and decrease in the ζ potential due to surface roughness [32]. Dukhin and Derjaguin provided experimental evidence for these seemingly contradicting phenomena [33]. They explained that this discrepancy is due to the electric double layer thickness relative to surface roughness. However, they did not elaborate on the cases where both are the same order. In this paper, we explore this regime using MD simulation.

III. PHYSICAL MODELS AND COMPUTATIONAL METHODS

Figure 1(a) shows the model system for a smooth wall nanochannel. It has charged and uncharged wall atoms, counterions (Na^+ ions), and water molecules. We modeled the walls as a simple cubic crystal structure and each wall atom as a charged/uncharged Lennard-Jones (LJ) atom, fixed at each lattice site. We determined the number of wall layers such that the thickness of the wall is just larger than the cutoff radius of the Lennard-Jones potential (7 Å). Therefore, for the smooth wall, there are four layers each in the upper wall and in the lower wall, but the number of layers

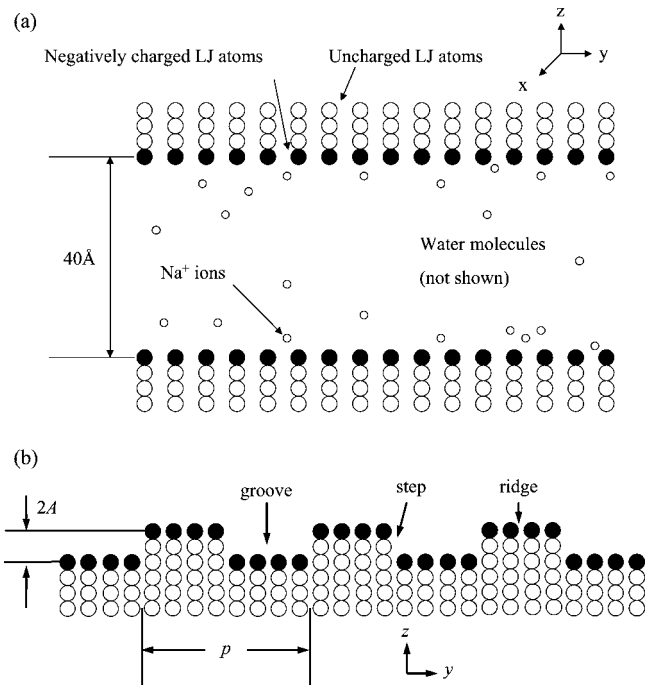

FIG. 1. (a) Model system for a smooth wall (● innermost layers). It includes charged and uncharged Lennard-Jones wall atoms, sodium ions, and water molecules. The coordinate system was defined as shown. (b) Model system for a rough wall. It has two-dimensional surface roughness with a spatial period p and an amplitude A. The flow region can be divided into the regions over the grooves and over the ridges.

varies with different types of surface roughness. The innermost layers [● in Fig. 1(a)] take uniform negative charges, corresponding to surface charge of $\sigma = -0.095$ C/m^2. All the other layers are electrically neutral. Since Freund [11] compared electro-osmotic flows for uniformly charged walls as well as for discretely charged walls and reported no significant difference for the two cases, we only simulated uniformly charged walls.

We constructed rough wall channels by adding extra partial layers of wall atoms to a smooth wall. As shown in Fig. 1(b), we modeled surface roughness as a sequence of two-dimensional subnanometer scale grooves and ridges along the flow direction, the y direction. Among many ways to construct rough walls, as summarized in Mo and Rosenberger [34], this is our choice for rough walls. In fact, it is somewhat like grooved channels in Kim *et al.* [28], but the amplitude of surface roughness in our models is equal to or less than surface roughness in microfabricated micro- or nanochannels. Therefore, we refer to it as surface roughness. Studying different shapes of surface roughness (such as a sinusoidal shape) should be an interesting topic for the future.

We can express the z coordinates of the wall atoms z_{wall} for the rough walls as

$$z_{\text{wall}} - z_{\text{wall,avg}} = A\Pi(2y/p), \tag{11}$$

where $z_{\text{wall,avg}}$ is the average location and $\Pi(y)$ is a step function-type function of period 1 defined by

TABLE I. Simulated physical models. A is an amplitude and p is the spatial period of surface roughness (see Fig. 1). k is the permeability of surface roughness, estimated using Eq. (13). We also simulated asymmetric wall channels for $A=0.9$ Å.

System	A [Å]	p [Å]	k [Å^2]	Symmetry
1	0	∞	0	Sym.
2 and 3	0.9	9.2	0.0054	Sym. and asym.
4 and 5	0.9	18.4	0.0054	Sym. and asym.
6 and 7	0.9	36.8	0.0054	Sym. and asym.
8	1.8	36.8	0.022	Sym.
9	2.7	36.8	0.049	Sym.
10	3.6	36.8	0.086	Sym.
11	4.5	36.8	0.14	Sym.

$$\Pi(y) = \begin{cases} 1 & \text{if } 0 < y < 1/2 \\ -1 & \text{if } 1/2 < y < 1. \end{cases} \tag{12}$$

We can thus specify surface roughness by an amplitude A and a spatial period p. Here the amplitude A corresponds to the root mean square (rms) roughness, the most common definition of surface roughness.

We defined the channel height as the difference in $z_{\text{wall,avg}}$ of the innermost layer in the upper wall and of the innermost layer in the lower wall. We fixed it at 40 Å for all the cases including a smooth wall channel. Indeed, the actual wall locations would not be the locations of the wall atoms since each wall atom has some finite volume. Nevertheless, we expect the effective channel height to be the same or very similar for all the cases.

As shown in Fig. 1(b), we can separate the entire flow region into the regions over the grooves and over the ridges, which have different channel heights locally. The flow behavior near the steps is expected to be complex due to the sidewalls.

We studied many different types of surface roughness with different values for A and p, as summarized in Table I. We also simulated asymmetric wall channels to compare to the symmetric cases. For all the cases, the surface porosity, ψ (defined as the fraction of a void volume in a surface porous "film" [32]), was 0.5. To estimate the permeability, k, for different types of surface roughness, we followed the Jenkins and Koenders approach [35], using Kozeny-Carman's permeability estimate,

$$k = \frac{D^2\psi^3}{150(1-\psi)^3}, \tag{13}$$

for porous medium with mean diameter D. For the length scale D, we used rms surface roughness, the same as A, as Jenkins and Koenders did in their paper [35].

We included only counterions for simplicity and computational efficiency. There are 20 Na^+ ions and 2067 water molecules in all the model systems. We modeled sodium ions as point charges with the Lennard-Jones potentials. For water molecules, we used the extended simple point charge model (SPC/E) [36].

TABLE II. Lennard-Jones parameters. We used the GROMOS-96 force field except for wall atoms whose parameters we took from Zhou *et al.* [12]. Between wall atom and the other types of atom, we applied the Lorentz-Berthelot combination rule.

Atom type	C_6 (kJ nm^6/mol)	C_{12} (kJ nm^{12}/mol)
O-O	2.62×10^{-3}	2.63×10^{-6}
Na^+-O	4.34×10^{-4}	2.35×10^{-7}
Na^+-Na^+	7.21×10^{-5}	2.10×10^{-8}
Wall-O	3.83×10^{-3}	3.29×10^{-6}
Wall-Na^+	6.45×10^{-4}	3.03×10^{-7}
Wall-wall	5.58×10^{-3}	4.06×10^{-6}

We used the GROMACS code [37] with the GROMOS-96 force field except for the wall atoms. The potential energy between two different atoms i and j, separated by r, can be expressed as

$$V_{ij}(r) = \frac{C_{12}}{r^{12}} - \frac{C_6}{r^{12}} + \epsilon\frac{q_i q_j}{r}. \tag{14}$$

The intended channel material was silica glass, and we took the Lennard-Jones parameters for wall atoms from Zhou *et al.* [12]. Their wall model is a united-atom Lennard-Jones model for SiO_2. Since we assumed simple cubic crystal structures for the walls, the nanochannels in our simulation have some limited degree of similarity with real glass channels. For the interactions of wall atoms with other types of atoms, we applied the Lorentz-Berthelot combination rule. The Lennard-Jones parameters for wall atoms, sodium ions, and oxygen atoms in water molecules are summarized in Table II.

For time integration, we used the Berendsen thermostat [38] combined with the standard Verlet integration algorithm with a time step of 1 fs. The time constant for the thermostat was 0.1 ps with the reference temperature of 300 K. We applied cubic periodic boundary conditions for all three directions. However, since our intended models are two-dimensional systems, we placed a vacuum space of 100 Å between the two periodic images in the z direction to have pseudo-two-dimensional systems in the xy plane. As mentioned above, the cutoff radius for the Lennard-Jones potential was 7 Å. For the calculation of electrostatic potentials, we adopted the particle-mesh Ewald (PME) method [39]. To constrain water molecules, we used the SETTLE algorithm [40], which provides an analytical solution for the case of water.

We first generated initial configurations by randomly distributing sodium ions in water slabs inside various nanochannels. We then performed energy minimization (the steepest descent algorithm) to avoid undesired van der Waals contacts. Before we start MD simulation, we assigned random numbers to initial velocities of water molecules and sodium ions according to a Maxwell distribution at 300 K. To equilibrate the model systems, we performed MD simulation during 0.5 ns without an electric field and were ready for pro-

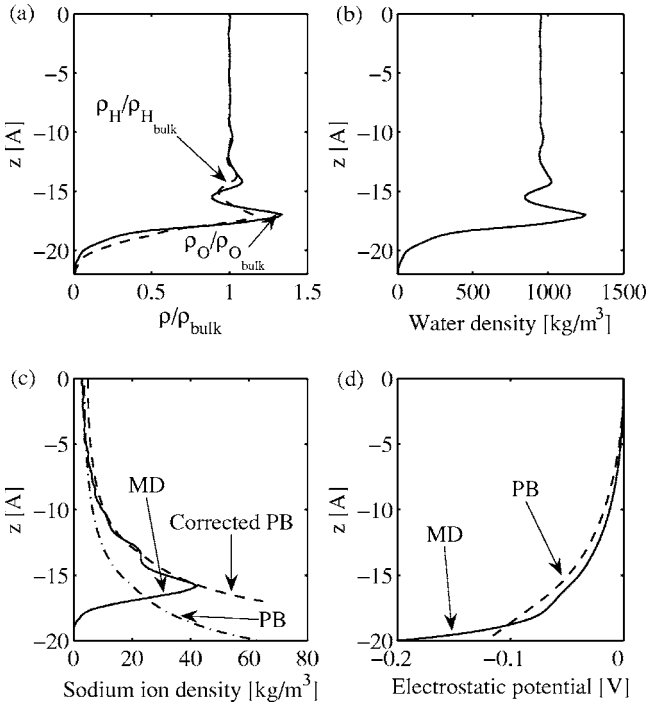

FIG. 2. One-dimensional profiles for a smooth wall. (a) Oxygen atom and hydrogen atom densities were normalized by their respective bulk values. (b) Water density profile. (c) Sodium ion density profiles obtained from MD simulation and PB solutions with two different boundary conditions (see text). (d) Profiles of electrostatic potential obtained from MD simulation and PB solution.

duction runs. Production runs lasted for 6 ns with and without an electric field. For the cases with an electric field (discussed in Sec. IV D), we sampled data for the final 5.5 ns after reaching steady state. The electric field strength applied in the y direction was 0.1 V/nm. The reason for this high electric field is to avoid relatively large thermal noises, which result in large statistical errors. With small electric fields, the convergence of the statistics should be very slow, which should lead to unacceptable computational time. The magnitude of an electric field in this work is about the same order as in previous works [11,13,22].

For all the computations except for the velocity autocorrelation functions (VACF) and the diffusion coefficients, we sampled data every 100 timestep, or every 100 fs. For the VACF and the diffusion coefficients, we sampled every timestep since the relevant timescale is in the order of 100 fs. For these calculations, production runs lasted for 60 ps after 500 ps equilibration due to the limitation of our data storage system.

IV. RESULTS AND DISCUSSIONS

A. Density profiles and electrostatic potential distributions

Figure 2 shows the density profiles of oxygen atoms, hydrogen atoms, water molecules, and sodium ions as well as the profile of the electrostatic potential along the z coordinate for the smooth wall. In Fig. 2(a), the densities for oxygen and hydrogen atoms were normalized with their bulk values (their mean values around the center of the channel, within 7 Å from the center). Figures 2(a) and 2(b) show layering of water molecules near the channel wall. The layering phenomenon near a solid surface (either charged or uncharged) has been reported in many previous works [13,16,18]. It was explained as a consequence of water attraction to the surface and of "volume exclusion" by Koplik and Banavar [41]. Precise patterns of water layering differ with different MD force fields, especially with different types of potential functions for wall-water interactions. In this work we found two pronounced peaks near the wall ($z \approx -17$ Å and -14 Å). At $z \approx -10$ Å, there is a third small peak and the density approaches the bulk value toward the center. Figure 2(a) shows normalized densities for oxygen and hydrogen atoms separately. The peak locations are slightly different for the two atoms, and their normalized peak values are also different. This is related to the preferred orientations of water dipole moments, which will be discussed in more detail in Sec. IV B.

Figure 2(c) shows the sodium ion density profile. The solid line is from our MD simulation; and the two other lines are from the solutions of the PB equation [Eq. (6)]. For the PB solutions, we used the Neumann boundary condition (see Sec. II) at two different locations, at $z=-20$ Å and $z=-17$ Å. The first corresponds to the location of the wall atoms, and the second corresponds to the location with which the PB solution has the best fit to the MD profile (we found the second location by repeatedly solving the PB equation with boundary conditions applied at different locations, each separated by 1 Å). The reason for applying a boundary condition at this shifted location is due to the finite size of ions and the wall. We can also find this finite size effect in the MD profile. The MD profile shows a peak value ~4 Å from the wall, not at the location of the wall atoms (the finite size effect was discussed in more detail in Qiao and Aluru [13]). From this location, the ion density profile decays toward the center, roughly showing a Boltzmann distribution. However, this decay is not monotonous but has a local maximum around 6 Å from the wall. This maximum corresponds to the valley between the first and second peaks in the water density profile. This correspondence was also found in previous studies [11,13,18]. Qiao and Aluru [13] explained it, stating that the energy required to insert ions in water density valley regions is lower than the energy required to insert ions in the bulk. It can also be explained with competing electrostatic attractions of water dipoles and ions as well as layering of water molecules [32].

Figure 2(d) shows the profile of the electrostatic potential both from the MD simulation and the PB solution. The PB solution, here and below, refers to the PB solution with the boundary condition at the shifted wall location, denoted by "Corrected PB" in Fig. 2(c). We calculated the MD electrostatic potential by solving the Poisson equation [Eq. (1)] with the MD ionic distribution. We used the dielectric constant computed from our MD simulation, which is not uniform in space and is quite different from the bulk value near the wall. We will discuss how we computed the dielectric constant in Sec. IV B. Although both the MD and PB profiles show exponential function-type profiles, one noticeable difference is that the MD slope is much steeper than the PB slope near the

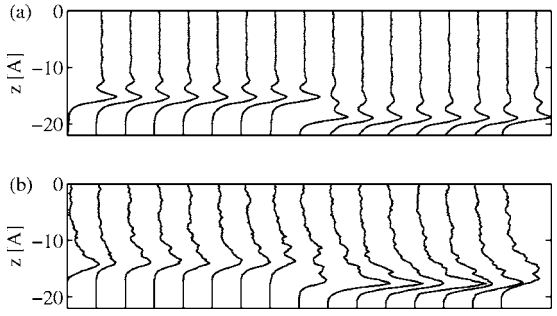

FIG. 3. Density profiles for the rough wall channel with symmetric surface roughness of a period of 36.8 Å and an amplitude of 1.8 Å. (a) Water density and (b) sodium ion density.

wall. The electrostatic potential around the center is similar to the two methods, but the value 20 Å from the center is around −200 mV with MD and around −120 mV with the PB. Although not shown here, the electrostatic potential profile obtained with the uniform bulk dielectric constant using the MD ionic distribution was very different from the MD profile here. Indeed, it was more similar to the PB profile than the MD profile.

We calculated density profiles for the rough wall channel. Figure 3 shows water and ion density profiles for the rough wall with symmetric surface roughness with a period of 36.8 Å and an amplitude of 1.8 Å. In both the water density profile and the ion density profile, the peak locations measured from the wall are about the same as for the smooth wall channel except near the step regions. Especially for water, the shape of the entire profile measured from the wall is very similar to the shape for the smooth wall, again with exceptions near the step regions.

We repeated density calculations for other types of surface roughness. The same trend (the similarity of profile shapes to those for the smooth wall) was found in all the cases. However, this similarity is less pronounced as the spatial period decreases or the amplitude increases. It is due to the increased influence of the step regions on the whole flow region since the step regions are frequent for the decreased period or the steps are steeper for the increased amplitude.

We computed the electrostatic potential profiles for different types of surface roughness, shown in Fig. 4. The inset shows the profiles inside the half channels and the main plot shows a zoomed-in view near the channel walls. These are all the MD results, using the same calculation procedure as for the smooth wall channel. We used a different nonuniform dielectric constant obtained for each model system. The overall shapes are all exponential function-type profiles, as shown in the inset, but the actual values deviate from one another, approaching toward the walls from the center. At the average wall atom location (i.e., $z=-20$ Å), the value varies significantly for different model systems, ranging between −130 and −220 mV. However, the variation decreases rapidly away from the wall, ranging, for example, between −100 and −130 mV (30% variation) at $z=-19$ Å. Since the wall atoms have some finite volume, determined by the Lennard-Jones potential, the actual wall locations (the surface locations) should not be the average wall atom locations but should be down further, toward the channel center. We thus

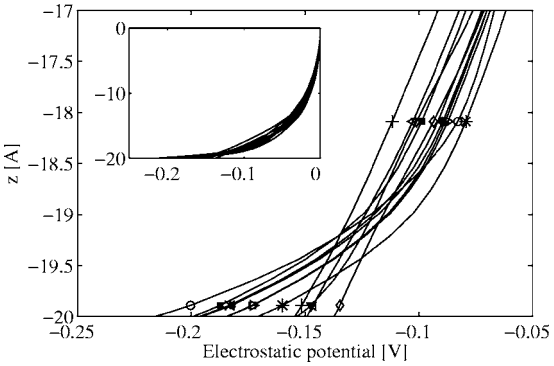

FIG. 4. Electrostatic potential profiles in different model systems. Note that data points are more frequent than symbols. Symbols: ◯ System 1, * System 2, ■ System 3, ▷ System 4, □ System 5, ● System 6, × System 7, ▽ System 8, ◇ System 9, ◁ System 10, + System 11.

expect the variation of the surface potential for different types of surface roughness to be less significant than that at $z=-20$ Å because the surface potential is defined at the actual wall location.

B. Polarization density and dielectric constant of water molecules

To further understand the structure of water molecules inside the smooth and rough wall channels, we computed the polarization density profiles of water molecules. We first computed the total dipole moment of water molecules in each bin, and then we normalized it by the bin volume to compute the polarization density of water molecules in each bin. The reason for this normalization is because the polarization density is independent of the bin volume while the total dipole moment is not. Figure 5(a) shows the components of the polarization density in three directions for the smooth wall. Near the wall, its z component is almost two orders of magnitude higher than the other two components,

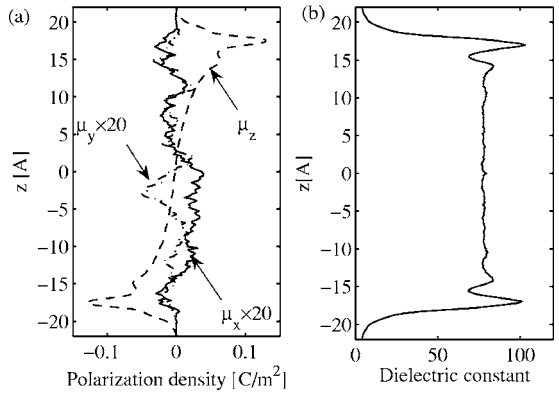

FIG. 5. (a) Polarization density profile of water molecules in three directions and (b) dielectric constant profile, both for the smooth wall channel. We calculated the total electric dipole moment of water molecules in each bin and normalized it by the bin volume to compute the polarization density shown. We calculated the dielectric constant using Eq. (15).

dominating its magnitude. Its profile shows two peaks each near the upper and lower walls and its magnitude is almost zero at the center. High values near the walls mean that water molecules are preferably oriented while small values near the center mean that they are isotropically oriented. This preferred orientation is such that hydrogen atoms inside each water molecule are preferably oriented toward the walls. The reason for this is as follows. Inside each water molecule, hydrogen atoms take positive charges and an oxygen atom take a negative charge and thus the direction of water dipole moment is from the oxygen atom location to the middle point of the two hydrogen atoms. The positive values near the upper wall indicate that the water dipoles are dominantly in the $+z$ direction (in fact, the orientation of water dipoles shows a probability density distribution, as reported in Freund [11]), meaning that hydrogen atoms are preferably oriented toward the wall. The opposite is true for the lower wall. This preferred orientation or "ordering" of water molecules near the wall was previously reported [11,18]. The ordering results in a deviation of the dielectric constant near the wall from the bulk values, which we will discuss in the next paragraph.

Figure 5(b) shows the profile of the dielectric constant for the smooth wall channel. In our MD simulation we computed the dielectric constant using a Clausius-Mosotti-type equation [42],

$$\epsilon_r = 1 + \frac{4}{3}\pi\rho\frac{1}{k_B T}g_k\mu^2. \tag{15}$$

Here ρ and T are the density and the temperature of dielectric medium, respectively. k_B is the Boltzmann constant and μ is the chemical potential. g_k is the Kirkwood factor defined as

$$g_k \equiv \frac{1}{N\mu^2}(\langle \boldsymbol{M}^2\rangle - \langle \boldsymbol{M}\rangle^2), \tag{16}$$

where N is the number of atoms in the system and $\boldsymbol{M}$ is the total dipole moment of the system. Note that Eq. (15) is valid for conducting boundary conditions [42]. To compute the dielectric constant profile, we used local values for the parameters appearing in the equations above, for example, the total dipole moment of water molecules in each bin for $\boldsymbol{M}$ and the number of water molecules in each bin for N. Zhou and Schulten took a similar approach [43]. This approach has two issues, the validity of boundary conditions and the use of local values. In fact, we obtained a value around 30 for the bulk, i.e., the mean value around the center of the channel. Zhou and Schulten also found a similar disagreement and listed a few possible reasons [43]. This disagreement is clearly an important scientific topic, but we circumvented this complex issue by normalizing our dielectric constant profile such that the mean value near the channel center (within 7 Å from the center) becomes the bulk value. We performed this normalization for all the cases and used the normalized dielectric constants for the electrostatic potential calculations shown in Figs. 2(d) and 4.

Figure 6 shows the two-dimensional profiles of the polarization density [Fig. 6(a)] and the dielectric constant for a rough wall channel [Fig. 6(b)]. Here the rough wall channel has symmetric surface roughness with a period of 36.8 Å and an amplitude of 4.5 Å. Compared to the profile for the smooth wall channel shown in Fig. 5(a), the profile in Fig. 6(a) shows a few differences. The maximum polarization density value inside the groove is ~10% higher than for the smooth wall although it may not be clear in the plot. It indicates that the ordering of water molecules is stronger than for the smooth wall. We also observed that the polarization density on the side walls is quite high. Indeed, we found a third peak band, which is absent for the smooth wall. Overall, the polarization density inside the grooves is high and this enhanced ordering might be due to more stagnant layers. We will discuss this more stagnant layer in Sec. IV C. Contrary to this enhanced ordering, the polarization density over the ridge is lower than for the smooth wall and thus water ordering is weaker. The dielectric constant profile shows a similar trend: increased values inside the grooves and decreased values over the ridges. This confirmed strong and weak ordering inside the grooves and over the ridges, respectively.

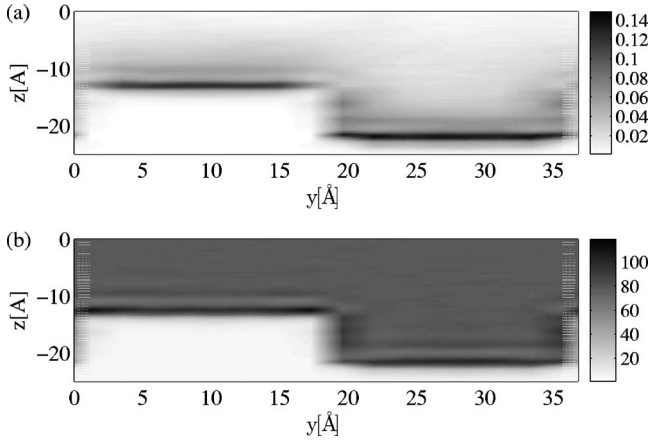

FIG. 6. Two-dimensional profiles for (a) the polarization density and (b) the dielectric constant of water molecules. The rough wall has symmetric surface roughness of a period of 36.8 Å and an amplitude of 4.5 Å.

C. Velocity autocorrelation function and diffusion coefficient

To understand transport phenomena of water molecules and sodium ions in nanochannels, we computed the velocity autocorrelation function (VACF) and the diffusion coefficient of water molecules and sodium ions. The autocorrelation function of a quantity A can be defined as

$$c_A(t) = \langle A(t)A(0)\rangle = \frac{1}{MN}\sum_{j=1}^{M}\sum_{i=1}^{N} A_i(t_j)A_i(t_j + t), \tag{17}$$

where N is the number of particles in the system and M is the number of time origins [44]. When A is a velocity, this autocorrelation function is related to the diffusion coefficient by

$$D = \frac{1}{3}\int_0^\infty c_v(t')dt'. \tag{18}$$

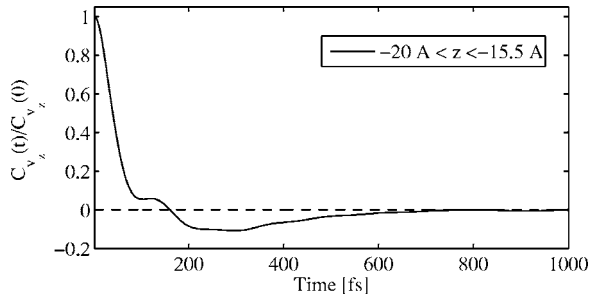

FIG. 7. Velocity autocorrelation function of water molecules in the first layer near the wall for the smooth wall. We normalized it by the value at $t=0$.

The diffusion coefficient can also be obtained in MD simulation using the Einstein relation,

$$3D = \lim_{t\to\infty} \frac{\langle |\boldsymbol{r}_i(t) - \boldsymbol{r}_i(0)|^2 \rangle}{2t}, \tag{19}$$

where $\langle |\boldsymbol{r}_i(t) - \boldsymbol{r}_i(0)|^2 \rangle$ is called the mean square displacement. In this article we used Eq. (18) to compute the diffusion coefficient.

Figure 7 shows the z directional normalized VACF of water molecules near the wall for the smooth wall nanochannel. We normalized the VACF by the value at $t=0$. It starts at 1 rapidly decreases to the negative value. After reaching the minimum value around $t=300$ fs, it slowly increases and oscillates and finally asymptotes to zero. The duration of time before reaching zero correlation value is the residence time, an average time during when molecules reside in a certain region (-20 Å$<z<-15.5$ Å in this case). In this paper, we defined the residence time as the time after when the normalized VACF is between -0.005 and $+0.005$.

Table III shows the residence time of water molecules in the first layer for the smooth and rough walls. We estimated the error to be $<1\%$ with a 95% confidence (all the subsequent error estimations were also with a 95% confidence). For the rough wall, we calculated the residence time for the flow regions over the ridge and for the flow region inside the groove, separately. The residence time for the groove is $\sim 20\%$ longer, and the one for the ridge is $\sim 12\%$ longer than for the smooth wall. The residence time is indicative of the adsorption of water molecules on the walls, so the increased residence time for the rough channel (over the ridge as well as inside the groove) means that more water molecules are adsorbed all over the rough wall. We initially expected longer residence time only for the groove, but we found that the residence time for the ridge is also longer than for the smooth wall. The reason for this is not quite clear but this might be due to the fact that the z directional movements of water molecules are suppressed as the channel height is locally lower than for the smooth wall.

TABLE III. Residence time of water molecules in the first layer near the wall ($|z-z_{\text{wall}}|<4.5$ Å). The rough wall has an amplitude of 4.5 Å and a period of 36.8 Å. For the rough wall, we calculated the residence time for the flow region over the ridge and the flow region inside the groove, separately. The estimated error is $<1\%$ with a 95% confidence.

		Rough	
Channel type	Smooth	Ridge	Groove
Residence time (fs)	715	768	858

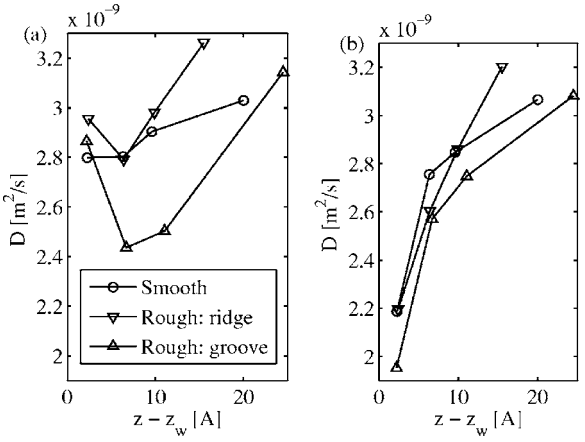

FIG. 8. Diffusion coefficient profiles of water molecules (a) in the xy plane and (b) along the z direction. The rough wall has symmetric surface roughness of a period of 36.8 Å and an amplitude of 4.5 Å. Note that the x axis in both the plots is the z-directional distance from the wall. The data points from the right correspond to the first, second, and third layers of water molecules and the bulk. The errors were estimated to be around 5%.

We computed the diffusion coefficient using the VACF [Eq. (18)]. Figure 8 shows the profile of the diffusion coefficient of water molecules in the xy plane and along the z direction. Around the center of the channel, the diffusion coefficients in the xy plane and those along the z direction are all roughly within the error range. The general trend both in Figs. 8(a) and 8(b) is that the diffusion coefficients decrease toward the wall. However, the z-directional diffusion coefficients near the walls are significantly reduced from the bulk values [Fig. 8(b)], whereas the variations for the xy plane are not that significant [Fig. 8(b)]. This anisotropy of the diffusion coefficients near the walls is consistent with the results of Lyklema *et al.* [17], where the "normal" viscosity was found to be increased by a factor of 4–5 from the bulk. The decreased diffusion near the wall can also be explained by the method of image, as explained in Happel and Brenner [45]. This result confirms the existence of a stagnant layer, or the Stern layer, as in Lyklema *et al.* [17]. They attribute this "stagnancy of liquids adjacent to solids" to "molecular layering of the solvents," which we also observed (see Sec. IV A). We also believe that the ordering of water molecules, discussed in Sec. IV B, contributes to this "stagnancy."

Figure 8(b) also shows that the z directional diffusivity in the first layer for the groove is smaller than the other two in the first layer. This indicates that the stagnant layer inside the groove is more stagnant than elsewhere, which is consistent with our finding: enhanced ordering of water molecules inside the groove (Sec. IV B) and long residence time of water molecules.

The xy-plane diffusivity in the second and third layers for the groove [Fig. 8(a)] is significantly low, although the dif-

TABLE IV. Diffusion coefficient of sodium ions for the smooth and rough walls. The rough wall has symmetric surface roughness of an amplitude of 4.5 Å and a period of 36.8 Å. The unit for the diffusion coefficient is 10^{-9} m^2/s. We estimated the errors to be $<8.5\%$.

	Smooth		Rough			
			Ridge		Groove	
Channel type	Bulk	~Wall	Bulk	~Wall	Bulk	~Wall
xy direction	1.20	1.24	1.44	1.49	1.40	1.25
z direction	1.34	0.940	1.23	1.18	1.41	0.849

fusivity in the first layer is a little higher than for the smooth wall (still within the error range). We think that this decrease is due to the sidewalls, as shown in Fig. 1. The reason why the diffusivity in the first layer is higher than in the second and third layers is not clear. It can be due to the fact that the discreteness of the wall perturbs the movement of water molecules and thus enhances diffusion in the *xy* plane, but we do not have a clear answer at present.

Table IV shows the diffusion coefficients of sodium ions. We estimated the sampling errors to be $<8.5\%$. Since the number of sodium ions is very small, we separated the flow region into two regions along the *z* direction: the bulk region and the region near the wall (within 5 Å from the wall). For the rough wall, we additionally separated the region along the *y* direction into the region over the groove and the region over the ridge. We found a similar trend to what we found for water molecules: (i) the anisotropy of diffusion near the walls, (ii) the decrease in the *z* directional diffusion inside the groove due to strong stagnancy, and (iii) low *xy* directional diffusion in the groove due to the sidewalls.

Up to this point, we presented our results of equilibrium MD simulation with no applied electric field. Here we briefly summarize our finding before presenting our nonequilibrium MD results. We first confirmed several of what previous studies have shown for the smooth wall: layering and ordering of water molecules near the wall [11,13,16,18], the anisotropy of water-ion mobility near the wall, and the existence of a stagnant layer near the wall [17]. For the rough wall we found that ordering is stronger inside the groove than for the smooth wall while layering is similar. We believe that this strong ordering is related to strong "stagnancy." To further understand this, we computed the residence time and the diffusion coefficient. These results show the increased residence time of water molecules and the decreased *z* directional diffusion inside the groove for the rough walls. We also observed that the *xy* directional diffusion is suppressed by the sidewalls. This will influence electro-osmotic flows in the *y* direction, which we will discuss in Sec. IV D.

D. Velocity profiles

From this section, we will present our results of nonequilibrium molecular dynamics (NEMD) simulation with applied electric fields. Since both the equilibrium and nonequilibrium simulation showed similar double layer structures (layering and ordering), we will not repeat discussions on density profiles, etc., obtained from our NEMD results.

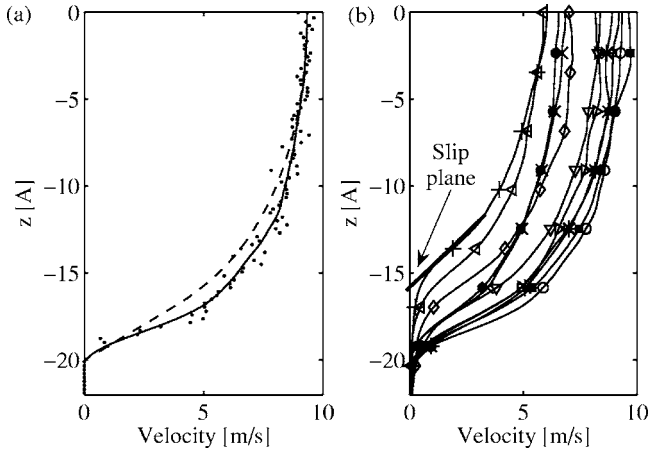

FIG. 9. Velocity profiles for (a) the smooth wall and (b) the rough walls. (a) The dots are actual data points from MD and the solid line is a line obtained by smoothing these data points. The reason for this smoothing is to reduce noises of our data points (thermal noises). The dashed line was obtained by solving the Stokes' equation with the ionic distribution, denoted by "Corrected PB" in Fig. 2(c). (b) All the solid lines are smoothed lines from the MD data for different types of surface roughness. Symbols are the same as in Fig. 4.

The velocity profile for the smooth wall is shown in Fig. 9(a) along with the continuum solution. The dots are actual data points from our MD results, and the solid line was obtained by smoothing these data points. As discussed in Sec. III, thermal noises are quite high and we used a running average to smooth the velocity profile in order to reduce these noises. The continuum solution (dashed line) was obtained by solving the Stokes' equation, as explained in Sec. II. For the ionic distribution, we used the one denoted by "Corrected PB" in Fig. 2(c), not the one denoted by MD. The figure shows that the solid line and the dashed line are reasonably similar, meaning that our MD velocity profile agrees well with the continuum solution. Both the profiles are roughly parabolic, indicative of overlapped electric double layers. This is to be expected since the channel height is comparable to the Debye length, which is 6.1 Å using

$$\lambda = \sqrt{\frac{\epsilon k_B T}{2e^2 n_\infty}}. \tag{20}$$

One-dimensional velocity profiles for different types of surface roughness are shown in Fig. 9(b). All the lines were again smoothed lines to reduce thermal noises. From this plot we can estimate the location of a slip plane for each model system. We first extrapolated the profile near the wall to obtain a straight line as shown in the figure. We then defined a slip plane as the *y* abscissa of this straight line for each model system. The locations of slip planes are important for computing the ζ potential (see Sec. IV E). The slip plane location is further apart from the wall as the amplitude increases or the period decreases.

The velocity vector field in the rough wall channel is shown in Fig. 10. We found that the velocity vectors are very

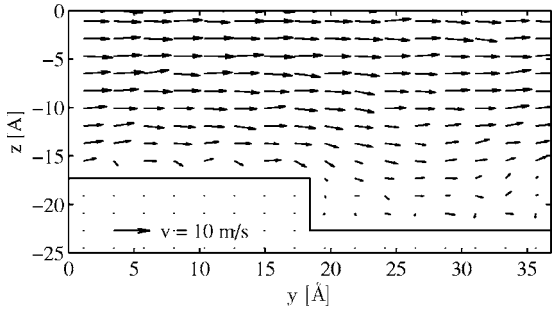

FIG. 10. Velocity vector field for the rough wall with symmetric surface roughness of a period of 36.8 Å and an amplitude of 2.7 Å.

small inside the groove, and they are uniformly aligned along the y direction elsewhere. This means that surface roughness effectively reduces the height of the channel. This reduced effective channel height is due to the decreased mobility of water molecules and sodium ions inside the groove, as discussed in Sec. IV C. Kandlikar *et al.* reported a similar "flow constriction" in their recent paper [46].

Figure 11 shows the dependency of the flow rate on surface roughness. Indeed, since we have periodicity in the x direction, we computed the flow rate per unit width Q', defined as

$$Q' \equiv \int_{z_{\text{lower}}}^{z_{\text{upper}}} v(z)dz, \tag{21}$$

where z_{upper} and z_{lower} indicate the upper and lower walls, respectively. We found that the flow rate depends on the amplitude and the period as well as the symmetry of surface roughness. Figure 11(a) shows that the flow rate at a small spatial period can be reduced by up to 17% even though the amplitude is fixed at 0.9 Å. Figure 11(b) shows the dramatic decrease of nearly 50% for the case of $A=4.5$ Å. The general trend is that the flow rate decreases as the period decreases or the amplitude increases. We also observed the effect of symmetry: the flow rates are lower for all the symmetric cases than for the asymmetric cases [Fig. 11(a)]. This is not a numerical artifact or a statistical error since we found the estimated error is smaller than 2%. The reason for the effect of symmetry is not clear at present and a more detailed analysis is necessary in the future.

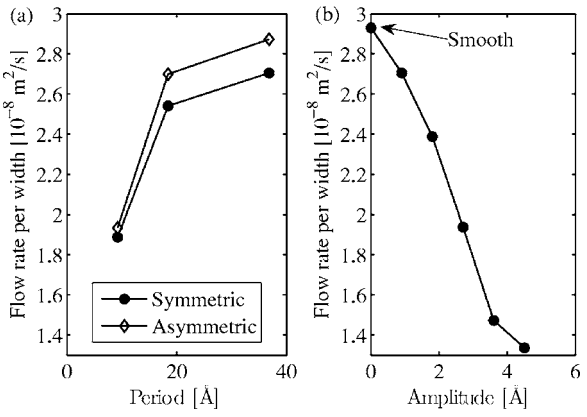

FIG. 11. Flow rate per unit width of the channel, Q', for (a) different periods of surface roughness and a fixed amplitude (0.9 Å) and (b) different amplitudes with a fixed period (36.8 Å). In (a), we simulated both the symmetric and asymmetric cases (as in Table I). The symmetry of surface roughness was defined with respect to the centerline of the channel.

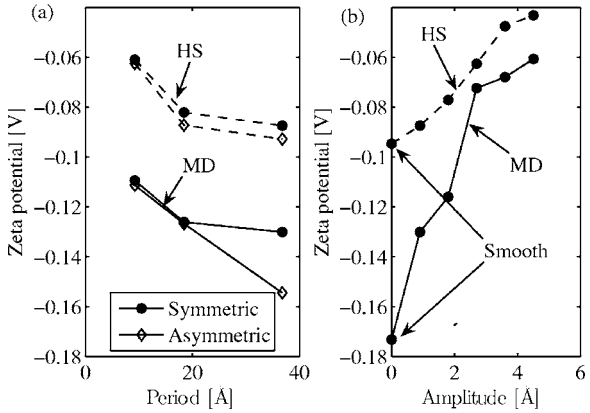

FIG. 12. ζ potential for (a) different periods of surface roughness and a fixed amplitude (0.9 Å) and (b) different amplitudes with a fixed period (36.8 Å). We computed the ζ potential in two ways, denoted by MD (molecular dynamics simulation) and HS (Helmholtz-Smoluchowski), which were described in more detail in the text. In (a), we simulated both the symmetric and asymmetric cases (as in Table I). The symmetry of surface roughness was defined with respect to the centerline of the channel.

E. ζ potential

Figure 12 shows the ζ potential for different types of surface roughness. We used two definitions for the ζ potential. The first definition, denoted by MD, is the electrostatic potential at the slip plane. The second one, denoted by HS was obtained using the so-called Helmholtz-Smoluchowski (HS) relation [29],

$$u_{\text{EOF}} = -\frac{\epsilon E \zeta}{\mu}. \tag{22}$$

Here we obtained u_{EOF} by volume-averaging of $v(z)$,

$$u_{\text{EOF}} \equiv \frac{1}{V}\int_V v(z)dxdy, \tag{23}$$

where V and A are the volume and the cross-sectional area, respectively.

Surprisingly, both approaches showed the same trend, that the absolute value of the ζ potential decreases as the amplitude increases or the spatial period decreases. We found that the absolute value of the ζ potential with the Helmholtz-Smoluchowski relation is smaller than the MD values for all the cases. We can explain this by realizing that the HS relation is valid for a plug-flow-type solution only, where there is no overlap of electric double layers.

From the MD results, we found that the ζ potential is more sensitive to the slip plane location than the electrostatic potential distribution. The locations of slip planes vary be-

tween 19.7 Å (system 1) and 15.8 Å (system 11) from the center while the electrostatic potentials change very rapidly within these locations. Indeed, the electrostatic potential changes from −173 to −61 mV there.

V. CONCLUSIONS

The density profile of water molecules for the smooth wall showed layering of water molecules near the wall. This layering along with the finite size effects of ions and the walls results in the departure of the counter-ion distribution from the PB solution. Similar layering was found for all the rough wall channels except near the step regions.

For the smooth wall, the electrostatic potential profile obtained with MD has a steeper slope near the wall than the PB profile. The surface potential, the electrostatic potential at the actual wall location, is within 30% range for all the model systems with different types of surface roughness.

To understand the orientation of water molecules, we computed the polarization density. Near the wall, its z direction component is two orders of magnitude higher than the other two components, indicating "ordering" of water molecules such that hydrogen atoms in each water molecule are oriented toward the wall. Inside the groove for the rough wall channels, the maximum magnitude of the polarization density is 10% higher than for the smooth wall and a third peak band is present. This enhanced ordering inside the groove is due to the more stagnant layer, which was confirmed by the results about the residence time and the diffusion coefficient. The dielectric constant, computed with a Clausius-Mosotti-type equation, also confirmed it.

Using the VACF, we computed the residence time and the diffusion coefficient of water molecules and ions. The residence time of water molecules in the first layer is longer for the rough wall than for the smooth wall. This means that more water molecules are adsorbed on the rough wall. The results on the diffusion coefficient of water molecules and sodium ions are (i) the anisotropy of diffusion near the wall, (ii) the decreased z directional diffusion inside the groove, and (iii) the lowered diffusion of water molecules and ions in the xy plane inside the groove. Especially, the lowered mobility inside the groove along the y direction partly explained decreasing flow rates for increasing amplitudes of surface roughness.

We also performed NEMD simulation to compute electroosmotic flows in nanochannels of different types of surface roughness. The velocity profiles are different from the plug flow profiles since the channel height is comparable to the Debye length. The velocity vector field for the rough channel showed that the flow inside the grooves is very small. Therefore, the flow rate was smaller for the increased amplitude of surface roughness. We also found that the flow rate decreases with the period of surface roughness and the flow rate for the asymmetric cases is larger than for the symmetric cases.

The ζ potential (absolute value) showed the same trend as the flow rate. We found that it is more sensitive to the slip plane locations than the electrostatic potential distributions since the latter change very rapidly near the wall.

ACKNOWLEDGMENTS

This research was funded by the Joint Research Initiative grant from the NASA Ames Research Center. We acknowledge all the valuable advice from Professor Juan G. Santiago at Stanford University.

[1] D. Stein, M. Kruithof, and C. Dekker, Phys. Rev. Lett. **93**, 035901 (2004).
[2] S. Pennathur and J. G. Santiago, Anal. Chem. **77**, 6782 (2005).
[3] U. Raviv, P. Laurat, and J. Klein, Nature (London) **413**, 51 (2001).
[4] R. Fan, Y. Y. Wu, D. Y. Li, M. Yue, A. Majumdar, and P. D. Yang, J. Am. Chem. Soc. **125**, 5254 (2003).
[5] N. R. Tas, J. Haneveld, H. V. Jansen, M. Elwenspoek, and A. V. D. Berg, Appl. Phys. Lett. **85**, 3274 (2004).
[6] Y. Gogotsi, J. A. Libera, A. Guvenc-Yazicioglu, and C. M. Megaridis, Appl. Phys. Lett. **79**, 1021 (2001).
[7] M. B. Stern, M. W. Geis, and J. E. Curtin, J. Vac. Sci. Technol. **15**, 2887 (1997).
[8] H. Daiguji, P. D. Yang, A. J. Szeri, and A. Majumdar, Nano Lett. **4**, 2315 (2004).
[9] D. Raabe, Modell. Simul. Mater. Sci. Eng. **12**, R13 (2004).
[10] N. G. Hadjiconstantinou and O. Simek, J. Heat Transfer **124**, 356 (2002).
[11] J. B. Freund, J. Chem. Phys. **116**, 2194 (2002).
[12] J. D. Zhou, S. T. Cui, and H. D. Cochran, Mol. Phys. **101**, 1089 (2003).
[13] R. Qiao and N. R. Aluru, J. Chem. Phys. **118**, 4692 (2003).
[14] C. Kleinstreuer and J. Koo, J. Fluids Eng. **126**, 1 (2004).
[15] E. Lauga, M. P. Brenner, and H. A. Stone, in *Handbook of Experimental Fluid Dynamics*, edited by J. Foss, C. Tropea, and A. Yarin (Springer, New York, 2005), Chap. 15.
[16] G. E. Karniadakis and A. Beskok, *Micro Flows* (Springer-Verlag, Berlin, 2002).
[17] J. Lyklema, S. Rovillard, and J. D. Coninck, Langmuir **14**, 5659 (1998).
[18] E. Spohr, J. Phys. Chem. **93**, 6171 (1989).
[19] E. Spohr, Electrochim. Acta **49**, 23 (2003).
[20] C. L. Rice and R. Whitehead, J. Phys. Chem. **69**, 4017 (1965).
[21] W. L. Qu and D. Q. Li, J. Colloid Interface Sci. **224**, 397 (2000).
[22] R. Qiao and N. R. Aluru, Phys. Rev. Lett. **92**, 198301 (2004).
[23] R. Qiao and N. R. Aluru, Colloids Surf., A **267**, 103 (2005).
[24] L. Joly, C. Ybert, E. Trizac, and L. Bocquet, Phys. Rev. Lett. **93**, 257805 (2004).
[25] M. Zembala, Adv. Colloid Interface Sci. **112**, 59 (2004), ISSN 0001-8686.
[26] Y. D. Hu, C. Werner, and D. Q. Li, Anal. Chem. **75**, 5747 (2003).
[27] Y. D. Hu, C. Werner, and D. Q. Li, J. Colloid Interface Sci.

280, 527 (2004).
[28] M. J. Kim, A. Beskok, and K. D. Kihm, Exp. Fluids **33**, 170 (2002).
[29] J. Lyklema, *Solid-Liquid Interfaces*, Vol. 2 of Fundamentals of Interface and Colloid Science (Academic Press, New York, 1995).
[30] *CRC Handbook of Chemistry and Physics* (CRC Press, Boca Raton, 2006).
[31] J. Israelachvili, *Intermolecular and Surface Forces* (Elsevier, New York, 1992).
[32] J. J. Bikerman, *Physical Surfaces* (Academic Press, New York, 1970).
[33] S. S. Dukhin and B. V. Derjaguin, *Electrokinetic Phenomena, Surface and Colloid Science*, Vol. 7, (Wiley, New York, 1974).
[34] G. Mo and F. Rosenberger, Phys. Rev. A **42**, 4688 (1990).
[35] J. T. Jenkins and M. A. Koenders, Granular Matter **7**, 13 (2005).
[36] H. J. C. Berendsen, J. P. M. Postma, W. F. Vangunsteren, A. Dinola, and J. R. Haak, J. Chem. Phys. **81**, 3684 (1984).
[37] D. V. D. Spoel, E. Lindahl, B. Hess, A. R. V. Buuren, E. Apol, P. J. Meulenhoff, D. P. Tieleman, A. L. T. M. Sijbers, K. A. Feenstra, R. V. Drunen *et al.*, *Gromacs User Manual Version 3.2* (University of Groningen, Groningen, 2004), www.gromacs.org
[38] H. J. C. Berendsen, J. R. Grigera, and T. P. Straatsma, J. Phys. Chem. **91**, 6269 (1987).
[39] T. Darden, D. York, and L. Pedersen, J. Chem. Phys. **98**, 10089 (1993).
[40] S. Miyamoto and P. A. Kollman, J. Comput. Chem. **13**, 952 (1992).
[41] J. Koplik and J. R. Banavar, *Continuum Deductions from Molecular Hydrodynamics* (Annual Reviews, Palo Alto, 1995), pp. 257–292.
[42] C. J. F. Böttcher, *Theory of Electric Polarization* (Elsevier, New York, 1973).
[43] F. Zhou and K. Schulten, J. Phys. Chem. **99**, 2194 (1995).
[44] A. R. Leach, *Molecular Modelling: Principles and Applications* (Pearson, Harlow, 2001).
[45] J. Happel and H. Brenner, *Low Reynolds Number Hydrodynamics: With Special Applications to Particulate Media* (Springer, New York, 1983).
[46] S. G. Kandlikar, D. Schmitt, A. L. Carrano, and J. B. Taylor, Phys. Fluids **17**, 100606 (2005).